Calculations of B_1 Distribution, SNR, and SAR for a Surface Coil Adjacent to an Anatomically-Accurate Human Body Model

Christopher M. Collins[1,3] and Michael B. Smith[1,2*]

Calculations of the radiofrequency magnetic (B_1) field, SAR, and SNR as functions of frequency between 64 and 345 MHz for a surface coil against an anatomically-accurate human chest are presented. Calculated B_1 field distributions are in good agreement with previously-published experimental results up to 175 MHz, especially considering the dependence of field behavior on subject anatomy. Calculated SNR in the heart agrees well with theory for low frequencies (nearly linear increase with B_0 field strength). Above 175 MHz, the trend in SNR with frequency begins to depend largely on location in the heart. At all frequencies, present limits on local (1 g) SAR levels are exceeded before limits on whole-body average limits. At frequencies above 175 MHz, limits on SAR begin to be an issue in some common imaging sequences. These results are relevant for coils and subjects similar to those modeled here. Magn Reson Med 45:692–699, 2001. © 2001 Wiley-Liss, Inc.

Key words: calculations; SNR; power; MRI; high field

The desire for a greater signal-to-noise ratio (SNR) in magnetic resonance spectroscopy (MRS) and imaging of humans continues to fuel interest in MR research at increasing static magnetic (B_0) field strengths, and consequently with increasing radiofrequency (RF) magnetic (B_1) field frequencies. As B_1 frequency increases, the spatial distribution of the B_1 field in a given object becomes more complex. This makes predictions of both SNR and the specific absorption rate (SAR) more difficult. Although at frequencies up to 64 MHz a nearly linear increase in SNR with B_0 field strength is expected theoretically (1–3) and seen experimentally (2) in human geometries, prediction of SNR at frequencies higher than this requires consideration of all of Maxwell's equations in 3D structures similar to those of interest in experiment (4–10).

Calculations of the B_1 field patterns, SAR, and SNR as functions of frequency for a surface coil used for both transmit and receive against the human chest are presented here. Calculations were performed in such a way as to make comparison to previous experiments (11) possible, and results of SAR calculations are presented in a manner that should make prediction of SAR in particular experiments with a similar coil and subject possible.

[1]Department of Radiology, Pennsylvania State University College of Medicine, Hershey, Pennsylvania.

[2]Department of Physiology, Pennsylvania State University College of Medicine, Hershey, Pennsylvania.

[3]Department of Bioengineering, University of Pennsylvania, Philadelphia, Pennsylvania.

*Correspondence to: Michael B. Smith, Center for NMR Research, NMR/MRI Building, Department of Radiology H066, Pennsylvania State University College of Medicine, 500 University Drive, Hershey, PA 17033.
E-mail: mbsmith@psu.edu

METHODS

A model of the human body for use with the finite difference time domain (FDTD) method of numerical calculation for electromagnetics (12,13) was created by first segmenting the digital photographic data of the National Library of Medicine's Visible Male Project, and then creating a 3D grid of Yee cells (13) from the segmented data. The images of the Visible Male Project, with a resolution of 1/3 mm in the left-right (x) and anterior-posterior (y) directions, were segmented at 5-mm intervals in the inferior-superior (z) direction by a fairly manual process, reference to anatomical atlases, and assistance from two practicing radiologists and one medical student. A program was written to create a 3D grid of Yee cell cubes from the segmented images with a spatial resolution of 5 mm in each dimension ($\Delta_x = \Delta_y = \Delta_z = 5$ mm). In a previous study of the relationship between spatial resolution and SAR levels, as calculated in the human head with the FDTD method (14), it was found that maximum local (1 cm^3) SAR values calculated with 8 cells per cm^3 ($\Delta_x = \Delta_y = \Delta_z = 5$ mm) were different from those calculated with 100 cells per cm^3 by less than 20%, and that average SAR values calculated with 8 cells per cm^3 were different from those calculated with 100 cells per cm^3 by less than 7%. Since the layer of skin is very thin in some places, and some information regarding it may be lost in the creation of a model with 5-mm dimensions, a second program was written to ensure that a continuous layer of skin existed by assigning the properties of skin to the surfaces of all Yee cell cubes that are adjacent to air. This step was seen as important because the conductivity of skin is greater than that of the fatty tissue beneath it in most places by a factor of about 10, and skin is typically the closest tissue to the RF coil elements. Thus SAR levels in the skin are generally expected to be relatively high in comparison to other tissues (15). Several slices through the completed model are shown in Fig. 1. In this figure each Yee cell cube (consisting of 12 Yee cell elements, one along each edge of the Yee cell cube) is depicted as a single box, and it appears that the skin is discontinuous in some areas, such as on the anterior surface in the second axial image from the right. Another view of this region showing all Yee cell elements (Fig. 2) reveals that the Yee cell elements representing skin on the outer surface here do indeed form a continuous layer. Values for material density were taken from the literature (16–19), and values for electrical properties were derived at each frequency by linear interpolation from measurements by Gabriel (20) in each tissue.

A circular surface coil with a diameter of 22.9 cm was modeled near the chest of the whole-body model. The coil was placed at a distance of 1 cm from the tissue. This 1-cm
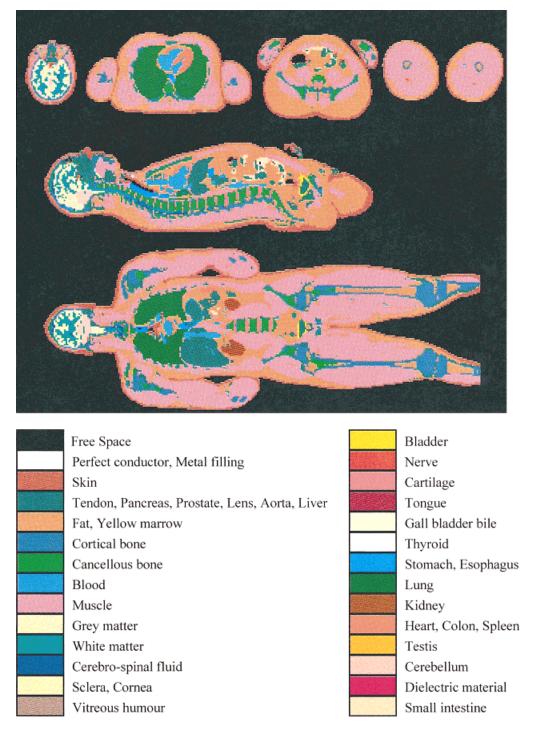
FIG. 1. Slices through a whole-body 3D model with 5-mm resolution in each dimension. Top: Axial slices through the head, thorax, abdomen, and thighs. Middle: Sagittal slice through the middle of body. Bottom: Coronal slice chosen to show the extent of the legs.

distance occurs where the pectoral muscles are more protrusive (left and right of center). Along the sagittal centerline (near the sternum), the distance between the coil and tissue is greater, with the greatest distance being almost 4 cm between the superior arc of the coil and the throat of the human body model. The coil model was driven with four voltage sources spaced evenly about the coil. The four voltage sources had identical magnitude and phase at each frequency. This is consistent with theoretical require-

ments for resonance of a symmetric four-capacitor coil, provided that the coil is loaded symmetrically and lengths of conductive segments are not long compared to one wavelength at the frequency of interest. This method can therefore be seen as an idealized approximation for this case with asymmetric loading, especially at frequencies of 260 and 345 MHz, where the length of the conductive segments is 0.156 and 0.207 times that of one wavelength, respectively. A surface coil of this size driven at only one
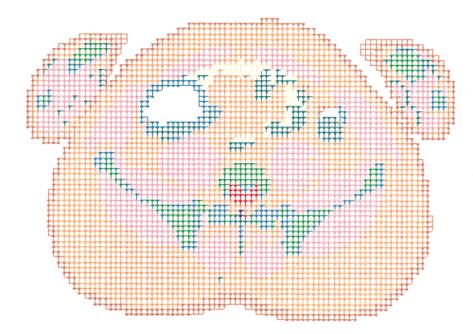
FIG. 2. In a view of an axial slice through the abdomen showing all Yee cell elements (*x*-oriented: horizontal lines, *y*-oriented: vertical lines, *z*-oriented: squares) it is apparent that not all Yee cell elements, such as the skin on the anterior surface of the abdomen, are shown when one Yee cell cube is displayed per pixel, as in Fig. 1.

location at 345 MHz would likely have a less symmetric field distribution than that shown here. Coils can be constructed and driven a number of different ways, however, and it is possible that a coil driven at more than one location could have a very similar field distribution to that shown here. For the purposes of this study, in which we attempted to examine the B_1 field distribution in the presence of a human sample and the effects of this distribution on MRI as functions of frequency, we preferred to keep the coil electrical behavior fairly constant. Electrical behavior of specific coils at these high frequencies, depending on location and number of drive points, type of capacitors (distributed or lumped-element), distance from the chest, and other design considerations should be the subject of future calculations.

All FDTD calculations were set up and performed with the aid of commercially-available software (XFDTD; Remcom, Inc., State College, PA). Calculations of steady-state B_1 fields and SAR were performed at 64, 125, 175, 260, and 345 MHz (corresponding approximately to B_0 field strengths of 1.5, 3.0, 4.0, 6.0, and 8.0 Tesla) with voltage source magnitudes equal to 1 volt. The complex (using phasor notation to include both magnitude and phase) RF electrical field (**E**) vector information and complex RF magnetic field (B_1) vector information at all vertices on the grid of Yee cells were derived from the FDTD calculation results. The amplitudes of the circularly-polarized components of the B_1 field on an axial plane through the chest were then calculated as (21):

$$B_1^+ = |(\hat{B}_x + i\hat{B}_y) \div 2| \qquad [1a]$$

and

$$B_1^- = |(\hat{B}_x - i\hat{B}_y)^* \div 2| \qquad [1b]$$

where $\hat{B}_x$ and $\hat{B}_y$ are complex values as denoted with a circumflex, i is the imagnary unit, the asterisk indicates the complex conjugate, and imaginary components are 90° out of phase with real components at the frequency of interest. Whether B_1^+ or B_1^- is the component that rotates in the direction of nuclear precession and thus induces the flip angle depends on whether the B_0 field is oriented with or against the *z*-axis. In this work it is assumed that B_1^+ is the flip-inducing component.
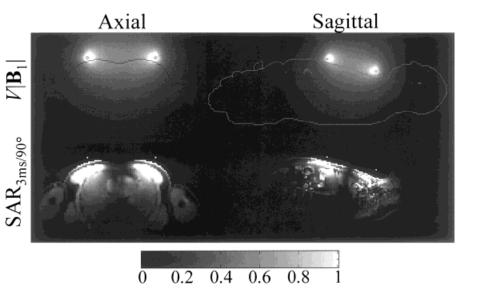
The dimensionless normalization factor, V, which is necessary to produce a normalized field magnitude, $V B_1^+$, equal to 1.957μT at a point approximately at the center of the heart, was determined at each frequency. This is the field strength necessary to produce a flip angle (α) of 90° in ^{1}H with a 3-msec rectangular RF pulse. Since B_1^+ is associated with driving voltages of 1 volt in the coil, the dimensionless normalization factor V is also equal to the driving voltage (in volts) necessary to produce the field pattern $V B_1^+$.

The available signal from a group of nuclei from a very small volume (cubic voxel, 5-mm dimensions) was assumed to be proportional to the square of the frequency of precession f (1,2), the sine of the flip angle in that volume, and the sensitivity of the coil to the local precessing nuclear magnetism, which is proportional to B_1^- (21). Noise from the sample (the dominant source of noise at these frequencies) is proportional to the square root of the power absorbed by the sample, P_{abs} (2). Thus, neglecting signal from protons in lipid and relaxation effects (T_1 and T_2) for simplicity, SNR at a point near the center of the heart was calculated at each frequency as (21):

$$\text{SNR} \propto f^2 \frac{|\sin(V B_{1c}^+ \gamma \tau) B_{1c}^-|}{\sqrt{P_{abs}}} \qquad [2]$$

where B_{1c}^+ is B_1^+ of the center voxel, τ is the duration of the rectangular pulse (assumed to be 3 msec in these calculations), and γ is the gyromagnetic ratio of ^{1}H. P_{abs}, the absorbed power over the entire body, is calculated for use in Eq. [2] as (13):

FIG. 3. Distributions of $V|\mathbf{B}_1|$ (top), and SAR$_{3msec/90°}$ (bottom) for body model near surface coil at 64 MHz. Gray scale expressed in terms of fraction of maximum scale value. Maximum scale value is 20μT for $|\mathbf{B}_1|$, and 4.05 W/kg (30 times whole-body average value) for SAR$_{3msec/90°}$. Values above scale maximum are expressed as the same (white) intensity as the scale maximum.

$$P_{abs} = \frac{1}{2} \sum_N (\sigma_{xn}E_{xn}^2 + \sigma_{yn}E_{yn}^2 + \sigma_{zn}E_{zn}^2)\Delta_x\Delta_y\Delta_z \quad [3]$$

where E_x, E_y, and E_z are the absolute magnitudes of the three orthogonal components of the electrical field E (calculated with the FDTD method), and σ is material conductivity. A dimensional analysis with σ having units of siemens/m, E having units of volts/m, and Δ_x, Δ_y, and Δ_z having units of meters shows the result to have units of watts. The subscript n indicates the nth voxel in the summation, and the subscripts x, y, and z indicate the orientation of the corresponding E field or σ components. The summation is performed over all N voxels in the human body model. Like B_1^+, the values of E and P_{abs} correspond to the fields where $V = 1$.

The SAR during the excitation with $V = 1$ in each voxel in the body model was calculated as (13):

$$SAR_{V=1} = \frac{\sigma_x}{2\rho_x}E_x^2 + \frac{\sigma_y}{2\rho_y}E_y^2 + \frac{\sigma_z}{2\rho_z}E_z^2 \quad [4]$$

where ρ is the material density (having units of kg/m³). The SAR during a 3-msec rectangular pulse resulting in a 90° flip at the center of the heart (SAR$_{3msec/90°}$) is equal to $V^2SAR_{V=1}$. For comparison with present limits on SAR (having units of watts/kg), the maximum SAR averaged over any one cm³ and the average SAR over the entire body model are presented here.

RESULTS AND DISCUSSION

The distribution of $V|\mathbf{B}_1|$ and SAR on two orthogonal planes through the center of the coil at 64 MHz are given in Fig. 3. At 64 MHz the field and SAR$_{3msec/90°}$ distributions are similar to what is expected at lower frequencies (22). Contour plots of the flip angle (α) distribution at each frequency are given in Fig. 4. Numerical values for the normalization factor V, resulting SAR$_{3msec/90°}$ levels (maximum 1 cm³ and whole-body average), P_{abs}, and SNR are given in Table 1. Line plots of average SAR$_{3msec/90°}$ and SNR as functions of frequency are given in Figs. 5 and 6.

Comparisons of calculated results in this work to previously-published results of Wen et al. (11) suggest that the trends in the B_1 field pattern and SNR with frequency calculated in a human sample are consistent with experiment—at least at frequencies up to 175 MHz. Determination of the accuracy of specific calculated quantities, especially SAR, will likely require further careful experiments and calculations.

Wen et al. (11) published B_1^+ maps made in two different human subjects with a 22.9-cm-diameter surface coil over the chest at 64 MHz (1.5T), 125 MHz (3T), and 175 MHz (4T). Despite differences in body shape and composition between their subjects and our model, calculated contours at $\alpha = 45°$, 90°, and 180° (Fig. 4) are similar in shape and position to experimentally mapped contours in subject 1 of the study by Wen et al. (Fig. 4 of Ref. 11). In comparing these studies it is important to note that the left-right convention in this work is like that used by radiologists: the "right" side of the model is on the viewer's left. This is the opposite of the convention used by Wen et al. Also, the plane used in calculations (including the atria and ventricular outflow tracts of the heart) may be a centimeter or two (at most) superior to that used in subject 1 of the study by Wen et al. (which apparently includes primarily the ventricles of the heart). Given the substantial differences between the experimentally-measured B_1^+ maps in the two subjects of the study by Wen et al., the presence of the 450° contour in calculations at 64 and 125 MHz (which is absent in subject 1 of the study by Wen et al.) may be attributable to the (apparently) larger pectoral muscles in the model. This will both cause the coil to be farther from the center of the heart than in the experiments by Wen et al., and will require the calculated B_1^+ field to penetrate through more muscle tissue, which is lossier than lung, bone, and fat. Thus higher B_1^+ values near the surface of our model may be necessary in order to achieve a 90° flip at the center of the heart.
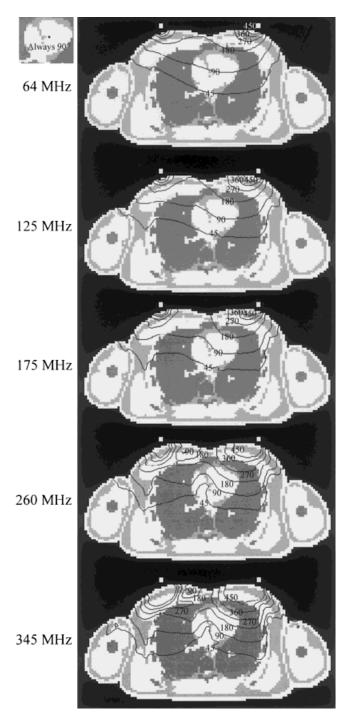
FIG. 4. Distribution of the flip angle α in chest as induced by a surface coil at several frequencies. Location of reference point (where $\alpha = 90°$ at all frequencies) shown in upper-left view of mediastinum. Contours at 45°, 90°, 180°, 270°, 360°, and 450° are labeled accordingly. Tissues are assigned one of three shades: dark (low-conductivity tissues, including bone and lung), medium (fat, also a low-conductivity tissue), and bright (high conductivity tissues, including skin, muscle, heart, aorta, blood, tendon, etc.). The location of the coil is shown with white dots. Note that the left-right convention used in radiology is used here: the model's "right" side is on the viewer's left. This is the opposite of the convention used by Wen et al. (11).

Table 1
Normalization Factor V, SAR Levels, Absorbed Power, and SNR at Center of Heart for Whole-Body Model With a Surface Coil (for 3 msec Rectangular Pulse Producing 90° Flip at Center of Heart)

Frequency (MHz)	V	$SAR_{3ms/90°}$ (W/kg)		$V^2 P_{abs}$ (W)	Relative SNR
		Max. one-cm^3	Average		
64	77.78	15.24	0.1349	12.91	1.000
125	158.3	58.41	0.4853	45.88	1.946
175	177.4	105.9	0.8883	83.65	2.713
260	378.3	309.8	2.731	200.6	3.895
345	533.8	774.0	6.130	557.0	5.021

Edelstein et al. (2) measured "intrinsic" SNR (ISNR) in the human head and in the human torso at several frequencies up to 64 MHz using linearly-driven volume coils. The results appeared to fall approximately along a straight line that intersected the origin. This agrees very well with calculations presented here for SNR in the torso using a surface coil at frequencies through 345 MHz (Fig. 6) at a location near the center of the heart. Experiments at frequencies of 64 MHz and below, however, are not necessarily good indicators of behavior much above 64 MHz because of the rapidly increasing complexity of the electromagnetic field spatial distribution at such frequencies (Fig. 4).

Both experiment (11) and the calculated results presented here suggest that at frequencies up to 175 MHz, SNR at the center of the heart should increase at a nearly linear rate in experiments using a surface coil near the chest. Our calculations indicate that at the center of the heart this nearly linear increase in SNR may continue to 345 MHz, but it is also important to examine the trend in SNR at locations other than what we have chosen as the center of the heart. At locations 2 cm anterior (location A), posterior (location P), left (reader's right: location L), and right (reader's left: location R) compared to the point at the center (location C), which is shown in Fig. 4 and used for all results presented up to now, the trend in SNR is shown
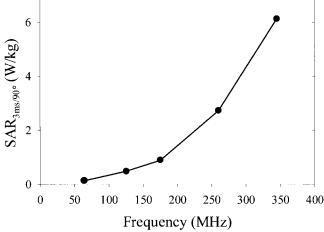

FIG. 5. Line plot of whole-body average $SAR_{3msec/90°}$ as a function of B_1 frequency.
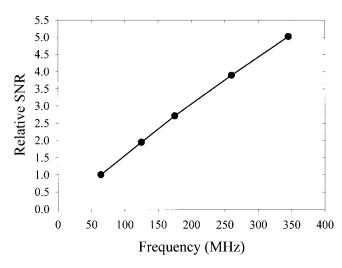
FIG. 6. Line plot of relative SNR as a function of B_1 frequency. Values are normalized to that at 64 MHz. A straight line passed through the two lowest-frequency points and extended towards the origin will very nearly pass through the origin. This suggests good agreement with theory and experiment at low frequencies (1–3).

FIG. 8. Line plot of relative SNR at several locations as a function of B_1 frequency when the flip angle is 90° at each respective location.

in Fig. 7 for the 90° pulse defined at location C, and in Fig. 8 for the 90° pulse defined at each respective location. Clearly, at frequencies much above 175 MHz the trend in SNR is very dependent on location due to the changing RF field distribution. Up to about 175 MHz, the SNR increases at an approximately linear rate at each location (Figs. 7 and 8). If the excitation pulse is defined such that the flip angle is 90° at location C, as the RF field distribution becomes more complex with increasing frequency (Fig. 4) the flip angle at neighboring locations will get farther from 90° and the SNR at these locations will become lower than that at location C (Fig. 7). If we calculate SNR as if the flip angle is 90° at each location for its respective data points so that
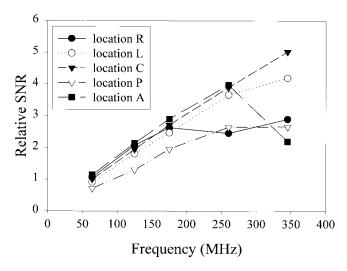

FIG. 7. Line plot of relative SNR at several locations as a function of B_1 frequency when the flip angle is 90° at location C. Locations are 2 cm anterior (location A), posterior (location P), left (reader's right: location L), and right (location R) compared to the point at the center (location C), which is shown in Fig. 4 and was used as the reference for results presented in Figs. 3–6 and Tables 1–2.
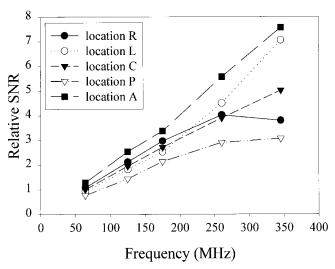
SNR is maximized at each location, we see that above 175 MHz the rate of increase (slope) may increase (locations A and L) or decrease (locations P and R) depending on how the RF field pattern changes with frequency (Fig. 8). A similar range of SNR behavior with frequency has been predicted for a body-sized phantom with an elliptical cross-section depending on material properties (4), for a spherical sample excited by a surface coil depending on sample size (8,9), and for a simple axis-symmetric model of the chest depending on model complexity (7).

Methods of assessing SAR in experiment generally rely on measurements of temperature made in homogeneous samples, or on assumptions about what the quality factor of the loaded and empty coil can reveal about the percent of applied power absorbed in the sample (23). While these methods may give a good estimate of the average SAR in a patient, they tell nothing about the distribution of the SAR or the magnitude of the maximum local SAR in a patient. The International Electrotechnical Commission (IEC) has suggested limits on average SAR in the head, average SAR in the body, and SAR in any 1-g region (24). The present limits for the normal operating mode are 1.5 W/kg over any 15 min for whole-body SAR, 3 W/kg averaged over any 10 min for average SAR over the head, and 8 W/kg in any gram of tissue in the head or torso (12 W/kg in any gram of tissue in the extremities) over any 5 min. With methods published previously (25) and the calculated SAR$_{3msec/90°}$ values in Table 1, it is possible to estimate the imaging parameters necessary to avoid exceeding the IEC limits in a number of possible experiments. The SAR levels induced during a pulse with flip angle α and duration τ would be:

$$SAR_{\tau/\alpha} = r\left(\frac{3ms}{\tau}\right)^2\left(\frac{\alpha}{90°}\right)^2 SAR_{3ms/90°} \qquad [5]$$

where r is a factor determined by the type of pulse used, calculated as a power ratio of the given pulse to a rectangular pulse with the same α and τ. If a rectangular pulse is

used, $r = 1.0$. If a Gaussian pulse is used, τ is defined as the full-width half-maximum of the Gaussian, and $r = 0.67$ (23). If a sinc pulse is used, τ is defined as the width of the central lobe at the zero crossings, and $r = 2.0$ (23). The SAR levels of a given pulse sequence will be equal to the sum of the energy absorbed from the pulses during the total image acquisition time divided by the total acquisition time. This can be written in general as:

$$ SAR = \frac{\sum_{n=1}^{N} (SAR_{\tau n/\alpha n} \times \tau n)}{TT} \qquad [6] $$

where αn and τn are the flip angle and pulse duration of the nth pulse in a sequence of N RF pulses, and TT is the total time necessary to acquire the image. Assuming the same N RF pulses are used in each repetition of a pulse sequence so that SAR over the total imaging time TT is equal to that over TR, we can calculate the minimum permissible TR to avoid exceeding some limit in SAR (SAR_{lim}) as:

$$ TR \geq \frac{\sum_{n=1}^{N} (SAR_{\tau n/\alpha n} \times \tau n)}{SAR_{lim}} \qquad [7] $$

where $SAR_{\tau n/\alpha n}$ can be calculated for any standard pulse type of duration τn and flip angle αn from the $SAR_{3msec/90°}$ values in Table 1 with Eq. [5]. Since for soft tissues (where conductivity and SAR are typically highest) the material density is very near 1 g/cm^3, the maximum SAR in one cm^3 will be very close to that for 1 g. The IEC normal operating mode limit for 1-g SAR in the body is greater than the limit for average SAR in the body by a factor of about 5.3. In Table 1 at every frequency the maximum 1-cm^3 SAR is greater than the whole-body average SAR by a factor of >100. Thus, in every case calculated here the local SAR level is the limiting factor for imaging parameters.

Assuming that only rectangular 90° and 180° pulses (flip angle defined at center of heart) are used, that 90° pulses have $\tau = 3$ msec and 180° degree pulses have $\tau = 6$ msec, it is possible to calculate the minimum allowable TR for a number of imaging sequences using 8 W/kg as SAR_{lim} and the maximum 1-cm^3 SAR levels in Table 1 for $SAR_{3msec/90°}$. The minimum allowable TR for several pulse sequences at several frequencies with these assumptions for a surface coil near a chest is given in Table 2. The values in Table 2 could be multiplied by appropriate factors to account for other pulse types and durations that might be used. These numerical results are technically only valid for the model and coil arrangement presented here. Nonetheless, these numbers may serve as a rough guide to what types of experiments should be possible at various frequencies with a large, muscular male subject and a surface coil on the chest. It appears that in experiments other than echo-planar imaging (EPI), gradient echo (GE), and spin echo (SE) sequences at 175 MHz and below, and perhaps the

Table 2

Minimum Allowable TR for Surface Coil on Chest With Several Pulse Sequences at Several Frequencies Assuming Only 3 msec Rectangular 90° and 6 msec Rectangular 180° Pulses Are Used

Frequency (MHz)	Minimum allowable TR (msec)				
	EPI	GE	SE	RARE 8	RARE 32
64	5.715	5.715	17.14	97.16	371.5
125	21.90	21.90	65.70	372.3	1242
175	39.71	39.71	119.3	675.1	2581
260	116.2	116.2	348.6	1975	7553
345	290.2	290.2	870.6	4933	18863

8-echo rapid acquisition with relaxation enhancement (RARE8) sequence at 64 MHz, SAR will be a consideration.

In these calculations the location of the maximum SAR in 1 g (cubic cm) of tissue occurs at nearly the same location at each frequency. This location is in the right medial portion of the pectoral muscle near the superior end of the sternum. This is interesting because this location is not the closest to the coil or to its voltage sources. We speculate that the SAR is highest here in this individual because the largest conductive bodies near the coil are the pectoral muscles, and since the thickness of these muscles diminishes as they approach the sternum, the current density will be increased in this region. In a subject with less pronounced pectoral muscles, this maximum might occur elsewhere. This emphasizes the importance of specific subject anatomy in determining the location of greatest SAR.

The FDA and IEC limits on SAR levels may change with time, but with the data and equations presented here it should be possible to estimate what imaging parameters are necessary to avoid exceeding future limits on SAR for coils and human geometries such as those modeled in this work.

CONCLUSIONS

Until recently, computational limitations have made calculations of SNR and SAR with increasing B_1 frequency impossible except in simple geometries. Here we have used numerical methods to predict SNR and SAR for a large, muscular male with a surface coil against his chest. Our calculations suggest that in this particular case, at frequencies above 175 MHz, SNR may increase or decrease with increasing B_1 frequency depending on the location and definition of the excitation pulse. This prediction is very dependent on the sample geometry and B_1 coil, as similar calculations for a head in a birdcage coil indicate that SAR and SNR will not pose problems at frequencies up to 8T (5). Clearly, there are major limitations and assumptions in these calculations. T_1, T_2, static field inhomogeneity, and a host of other factors are not considered. Still, in looking for fundamental relationships due to RF field behavior, the methods used here are well understood and generally accepted (2–9).

here, and to Harvey E. Smith, A.B., for his assistance in segmentation. We have benefited greatly from enlightening discussions and correspondence with Dr. David I. Hoult, including rigorous proofs of the necessary equations for calculating detected signal.

REFERENCES

1. Hoult DI, Lauterbur PC. The sensitivity of the zeugmatographic experiment involving human samples. J Magn Reson 1979;34:425–433.
2. Edelstein WA, Glover GH, Hardy CJ, Redington RW. The intrinsic signal-to-noise ratio in NMR imaging. Magn Reson Med 1986;3:604–618.
3. Hoult DI, Chen C-N, Sank VJ. The field dependence of NMR imaging: ii. arguments concerning an optimal field strength. Magn Reson Med 1986;3:730–746.
4. Ocali O, Atalar E. Ultimate intrinsic signal-to-noise ratio in MRI. Magn Reson Imaging 1998;39:462–473.
5. Collins CM, Smith MB. Calculated B_1 homogeneity, SNR, and SAR vs. frequency for an idealized quadrature birdcage coil. In: Proceedings of the7th Annual Meeting of ISMRM, Philadelphia, 1999. p 417.
6. Collins CM, Smith MB. Calculated SNR and SAR vs. frequency for a surface coil on the human chest. In: Proceedings of the7th Annual Meeting of ISMRM, Philadelphia, 1999. p 418.
7. Singerman RW, Denison TJ, Wen H, Balaban RS. Simulation of B_1 field distribution and intrinsic signal-to-noise in cardiac MRI as a function of static magnetic field. J Magn Reson 1997;125:72–83.
8. Carlson JW. Radiofrequency field propogation in conductive NMR samples. J Magn Reson 1988;78:563–573.
9. Keltner JR, Carlson JW, Roos MS, Wong STS, Wong TL, Buddinger TF. Electromagnetic fields of surface coil *in vivo* NMR at high frequencies. Magn Reson Med 1991;22:467–480.
10. Hoult DI. Sensitivity and power deposition in a high-field imaging experiment. J Magn Reson Imaging 2000;12:46–67.
11. Wen H, Denison TJ, Singerman RW, Balaban RS. The intrinsic signal-to-noise ratio in human cardiac imaging at 1.5, 3, and 4 T. J Magn Reson 1997;125:65–71.
12. Yee KS. Numerical solution of initial boundary value problems involving Maxwell's equations in isotropic media. IEEE Trans Ant Propag 1966;14:302–307.
13. Kunz KS, Luebbers RJ. The finite difference time domain method for electromagnetics. Boca Raton: CRC Press; 1993.
14. Collins CM, Smith MB. FDTD grid resolution and accuracy in SAR calculations for MRI. In: Proceedings of the 7th Annual Meeting of ISMRM, Philadelphia, 1999. p 2051.
15. Jin JM, Chen J, Chew WC, Gan H, Magin RL, Dimbylow PJ. Computation of electromagnetic fields for high-frequency magnetic resonance imaging applications. Phys Med Biol 1996;41:2719–2738.
16. Wlodzimierz E, Gos T. Density of trunk tissues of young and medium age people. J Biomech 1990;23:945–947.
17. Huang HK, Wu SC. The evaluation of mass densities of the human body in vivo from CT scans. Comput Biol Med 1976;6:337–343.
18. Cho ZH, Tsai CM, Wilson G. Study of contrast and modulation mechanisms in x-ray/photon transverse axial transmission tomography. Phys Med Biol 1975;20:879–889.
19. Clauser CE, McConville JT, and Young JW. Weight, volume, and center of mass of segments of the human body. Aerospace medical research laboratory, Wright-Patterson Air Force Base, Ohio: AMRL-TR-69-70; 1969.
20. Gabriel C. Compilation of the dielectric properties of body tissues at RF and microwave frequencies. Air Force materiel command, Brooks Air Force Base, Texas: AL/OE-TR-1996-0037; 1996.
21. Hoult DI. The principle of reciprocity in signal strength calculations—a mathematical guide. Concepts Magn Reson 2000;4:173–187.
22. Bendall RM. Surface coil technology. In: Partain CL, Price RR, Patton JA, Kulkarni MV, James Jr AE, editors. Magnetic resonance imaging. Philadelphia: WB Saunders; 1988. p 1201–1268.
23. Bottomley PA, Redington RW, Edelstein WA, Schenck JF. Estimating radiofrequency power deposition in body NMR imaging. Magn Reson Med 1985;2:336–349.
24. International Electrotechnical Commission. Medical electrical equipment, part 2: particular requirements for the safety of magnetic resonance equipment for medical diagnosis. IEC 601-2-33; 1995.
25. Collins CM, Li S, Smith MB. SAR and B_1 field distributions in a heterogeneous human head model within a birdcage coil. Magn Reson Med 1998;40:847–856.